Structural Evolution of $Li_xMn_2O_4$ in Lithium-Ion Battery Cells Measured In Situ Using Synchrotron X-Ray Diffraction Techniques

S. Mukerjee,* T. R. Thurston,* N. M. Jisrawi, X. Q. Yang,* and J. McBreen*

Brookhaven National Laboratory, Departments of Applied Science and Physics, Upton, New York 11973, USA

M. L. Daroux* and X. K. Xing*

Gould Electronics, Eastlake, Ohio 44095-4001, USA

ABSTRACT

We describe synchroton based X-ray diffraction techniques and issues related to in situ studies of intercalation processes in battery electrodes. We then demonstrate the utility of this technique, through a study of two batches of $Li_xMn_2O_4$ cathode materials. The structural evolution of these spinel materials was monitored in situ during the initial charge of these electrodes in actual battery cells. Significant differences were observed in the two batches, particularly in the intercalation range of $x = 0.45$ to 0.20. The first-order structural transitions in this region indicated coexistence of two cubic phases in the batch 2 material, whereas the batch 1 material showed suppressed two-phase coexistence. Batch 2 cells also indicated structural evolution in the low-potential region below 3.0 V in contrast to the batch 1 material. Differences in structural evolution between batches of $Li_xMn_2O_4$ could have important ramifications in their cycle life and stability characteristics.

Introduction

The low cost, high operating voltage, and low toxicity of spinel $Li_xMn_2O_4$ make it a good candidate for use as a cathode in rechargeable lithium-ion battery cells. However, this material cannot yet be reproducibly manufactured, a problem which arises in large part because the structural properties of $Li_xMn_2O_4$ vary considerably with synthesis conditions.[1-5] The structure also changes as the lithium is inserted and removed,[5-8] so studies of operating battery cells may help resolve some of these issues by allowing one to separate structural properties dependent on the Li content from those dependent on the underlying manganese-oxygen skeleton. In this paper we describe how synchrotron X-ray diffraction techniques can be applied to this research problem, and report some of our initial results from combined electrochemical and in situ X-ray diffraction measurements of lithium-ion "rocking chair" cells.

Early ex situ X-ray diffraction studies of $Li_xMn_2O_4$ were performed by Ozhuku, et al.[5] They found that two cubic phases coexist for $0.27 < x < 0.60$, a single cubic phase is present for $0.60 < x < 1.0$, and a cubic and tetragonal phase coexist for $1.0 < x < 2.0$. More recently Xia and Yoshio[6] have performed ex situ X-ray diffraction studies on $Li_xMn_2O_4$ cathode materials prepared under a variety of conditions. They found that structural behavior during lithium intercalation varies considerably depending on how the starting cathode material is prepared. Specifically, they demonstrated that the structural transition into two-phase coexistence is suppressed in cathode material that is prepared "lithium rich" or "oxygen rich," i.e., $Li_{1+x}Mn_{2z}O_{4+y}$ ($x \geq 1$, $y > 0$).

There have been a number of recent in situ X-ray diffraction studies on lithium battery cathode materials.[7-10] The $Li_xMn_2O_4$ measured by Richard et al.[8] exhibited two-phase coexistence behavior similar to that observed by Ozhuku et al.[5] and the suppression of the two-phase coexistence in the "oxygen rich" samples was observed in situ by Amatucci et al.[7] In situ X-ray diffraction studies of lithium cathode materials other than $Li_xMn_2O_4$ have also been done.[9-10] Li, et al.[9] performed in situ X-ray diffraction experiments on Li_xNiO_2 cathodes during the initial charge cycle, and Amatucci et al.[10] characterized the structural properties of Li_xCoO_2 for $0 < x < 1$. In all of these studies, various features in the voltage-capacity curve could be directly correlated with the structural changes in the cath-

* Electrochemical Society Active Member.

ode material. Thus, unique information for relating electrochemical and electrode structural properties can be provided by this technique. In situ X-ray scattering studies can provide other types of new information as well. For example, Amatucci et al.[10] also found that the end member of the Li_xCoO_2 series, CoO_2 is a structurally stable compound in their electrochemical studies, whereas CoO_2 had previously not been successfully synthesized.

There are difficulties in applying X-ray diffraction techniques to the study of battery cells. X-ray compatible cells typically have a specialized construction in order to allow illumination of the electrode materials, and in the work mentioned above, the X-rays enter the cell through beryllium windows. The problem with this approach is that beryllium windows can be difficult to seal and that beryllium becomes reactive at potentials greater than ~4.0 V. In order to circumvent these problems, the cell is typically designed such that no electrolyte comes in contact with the beryllium window. Such cells can therefore be awkward to handle, and cannot have exactly the same configuration as commercial cells. Another potential problem with the conventional in situ X-ray diffraction experiments is that they are nearly always performed in the reflection geometry. This causes the X-rays to penetrate only a few microns into the surface of the electrode material under study, as we describe in the detail below. Although it may not affect the results of a particular experiment, an experimental configuration wherein the entire bulk of the cathode material is probed is preferable, particularly in an intercalation process.

In this work, we circumvent many of the problems associated with previous in situ X-ray diffraction studies by utilizing highly penetrating hard X-rays from a synchrotron source.[11] This has allowed us to use cells with no special modifications such as beryllium windows or o-ring seals, to perform the diffraction experiments in transmission geometry so that the entire bulk of the electrode material is probed, and to perform experiments with much higher resolution and data-collection rates. We illustrate the utility of this approach through in situ studies of the structural evolution of $Li_xMn_2O_4$ cathode material in lithium-ion cells during the charging process.

Experimental

Synchrotron X-ray diffraction.—There are a number of factors that determine the signal rate in an X-ray diffraction experiment including the incident photon flux, the amount of X-ray absorption, the efficiency of the mono-

chromator and analyzer crystals, the size of the illuminated sample volume, and the scattering cross section itself. We begin this section by considering these various factors in relation to synchrotron and conventional X-ray diffraction experiments.

The brightness of synchrotron X-ray sources is not only considerably higher than that of conventional sources, but also covers a continuous band of photon energies. Figure 1 compares the brightness of a bending magnet beamline at the National Synchrotron Light Source (NSLS) to conventional sources that utilize Cu or Mo K_α emission lines. The conventional sources span a range of brightness, depending whether they are weaker tube or stronger rotating-anode sources. Even the brightest conventional sources are ~1000 times dimmer than a bending magnet beamline, however. At first glance the synchrotron data curve in Fig. 1 would seem to suggest that the optimal X-ray energy is ~8 keV, since the synchrotron source brightness is largest there. However as we discuss below, other factors, in particular the absorption of the sample, tend to favor higher energies.

The absorption X-rays can play a decisive role in determining the signal rate in a diffraction experiment. The basic equation for X-ray absorption is

$$I = I_0 \exp(-z/l) \qquad [1]$$

where I is the X-ray after passing through a thickness z of material, I_0 is the incident X-ray flux, and l is the penetration depth for the material in question. A key observation behind this study is that the penetration depth l is highly dependent on the energy of the incident X-ray photons. Figure 2 shows the penetration depth as a function of photon energy for $LiMn_2O_4$. At low X-ray energies the penetration depth is relatively small, but as the energy is increased, the penetration depth increases considerably. This increase coupled with the exponential dependence of eq 1, can lead to dramatic increases in signal rates.

Besides the incident photon energy, the scattering geometry employed also plays a role. In the symmetric reflection geometry (Fig. 3 (a)) the arrows labeled K_i and K_f represent the momenta of the incident and scattering photons, respectively. Considering the scattering intensity from identical volume elements at different depths z within the electrode material, the relative diffraction intensity from a given volume element depends on the total path length traversed by the incident and scattered X-rays. For the reflection geometry illustrated in Fig. 3 (a), the path
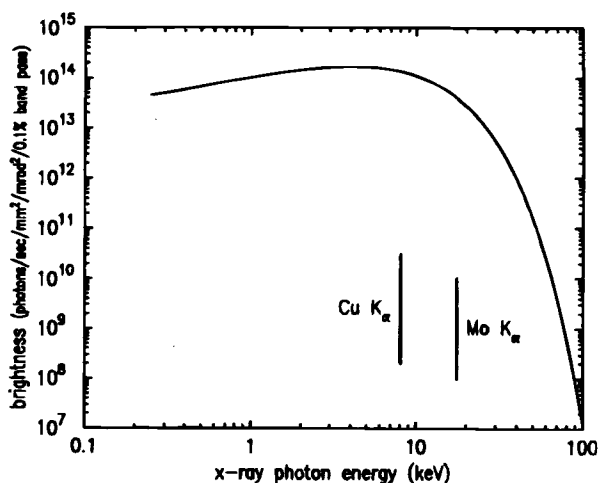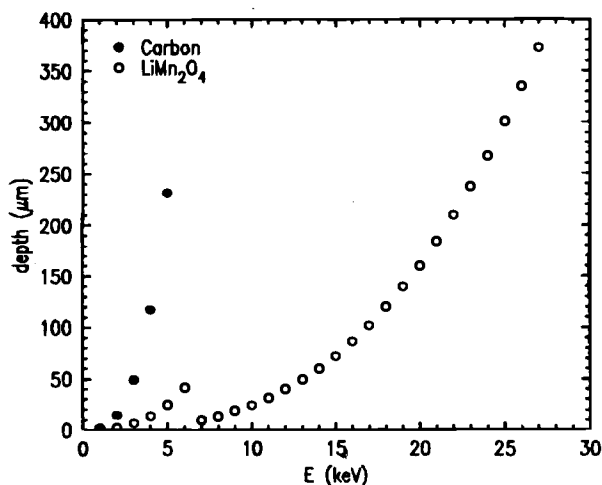

Fig. 2. Adsorption penetration depth for $LiMn_2O_4$ as a function of X-ray photon energy.

length r depends on the depth of the volume element z and the diffraction angle θ

$$r(z) = 2z/\sin(\theta) \qquad [2]$$

The depth z_{atten} at which the diffraction signal is attenuated by a factor e^{-1} is therefore

$$z_{atten} = l \sin(\theta)/2 \qquad [3]$$

In a conventional reflection geometry experiment done with 8 keV X-rays, the (531) $LiMn_2O_4$ Bragg peak occurs at $2\theta \sim 67°$ and $l \sim 14$ μm, so the effective penetration depth into the electrode material is ~3.9 μm. Of course, the binding materials and the electrolyte will have somewhat dif-
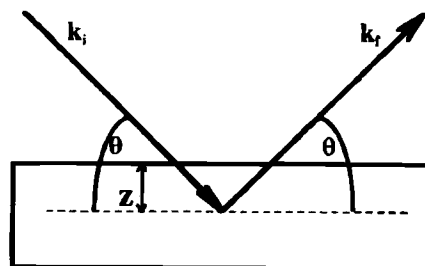
(*i*)
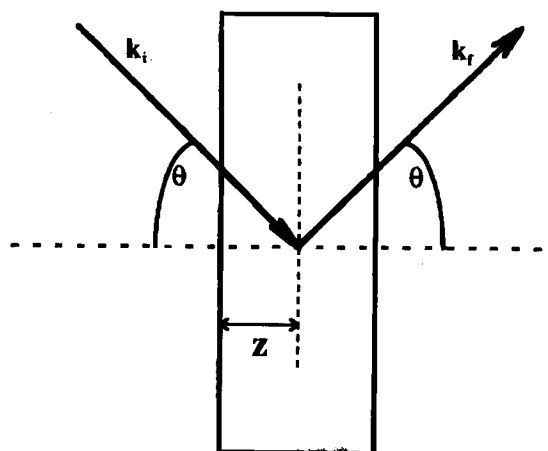
(*ii*)

Fig. 3. Scattering in a (*i*) symmetric reflection and (*ii*) symmetric transmission geometry. For both these scattering geometries, the rotation angle of the sample set at 1/2 of the scattering angle.

Fig. 1. Comparison of the brightness of an NSLS bending magnet and conventional sources with copper and molybdenum K_α anodes. The conventional sources have a range of brightness that depends on the configuration of the device and its power.

ferent X-ray penetration depths than $LiMn_2O_4$, but the general conclusion one can draw from this calculation is that X-rays probe only the material within a few microns of the surface in a conventional experiment. This near-surface region may or may not reflect the behavior of the bulk of the electrode material, so conventional in situ X-ray diffraction measurements must be interpreted with caution, particularly in intercalation studies.

The z penetration depth of the symmetric reflection geometry experiments does not increase substantially at larger X-ray energies. For 25 keV X-rays, the $LiMn_2O_4$ penetration depth l increases to ~300 μm, but the (531) $LiMn_2O_4$ Bragg peak occurs at a lower angle, $2\theta \sim 20.6°$. Under these conditions, z_{attn} still is only 27 μm, which is larger than the z penetration with 8 keV X-rays, but still considerably smaller than the thickness of a typical electrode.

In the symmetric transmission geometry (Fig. 3 (b)), the path length through which an X-ray photon travels within the material is independent of z, so the spectra is normalized over the bulk of the electrode. This is the primary advantage of this scattering geometry. The main disadvantage is that the X-rays must also travel through both electrodes, separator, electrolyte, and both the window materials in the end plates of the cell. Hence the highly penetrating X-rays from a synchrotron source are preferable for this type of an experiment.

The X-ray diffraction experiments to be described below were both done in the transmission geometry on cells without beryllium windows or other special modifications for X-ray diffraction work. Two different NSLS beamlines with quite different optics were used, X27A and X22A.

The experiments at X27A were done with 24.75 keV X-rays ($\lambda = 0.50$ Å) using a setup that is described briefly in a previous publication.[11] For these experiments, the extremely high resolution offered by the standard silicon crystals is not necessary, since the crystalline perfection of the $Li_xMn_2O_4$ material itself is not good. It is also possible to improve the signal intensity substantially by coarsening the instrumental resolution. For these reasons we used a LiF (200) analyzer crystal (~0.05° FWHM) and a Si (111) bent Laue (transmission geometry) monochromator in the instrumental setup.

The particular monochromator design utilized is relatively new.[12] Since this monochromator operates in a transmission geometry, it is useful only at high photon energies where the absorption of X-rays by silicon is minimal. The monochromatic flux is increased over that of a flat silicon crystal operating in a reflection geometry primarily for two reasons: (*i*) The angular acceptance is increased to match the natural divergence of the X-ray beam. For the NSLS ring, the beam divergence in the vertical direction is 0.006° full width at half-maximum (FWHM), whereas the Darwin width of a Si (111) reflection is 0.001° FWHM at 24.5 keV, so one can increase the flux by a factor of ~6 from this effect; and (*ii*) by bending the monochromator crystal, a range of *d-spacings* are created, and the energy bandpass of the monochromatic beam is increased.

The increase in the angular and energy bandpass, along with the better match between instrumental and sample resolution properties, lead to significant increases in signal rates. Compared to a conventional flat Si (111) crystal operating in a reflection geometry, sample peak intensities increased by over a factor of 100 when using our bent Laue monochromator. Obviously, this signal increase greatly facilitates the experiments.

The experiments at X22A were done with 10.33 keV X-rays ($\lambda = 1.2$ Å) using a more conventional X-ray diffraction beamline setup. The beamline contains a number of optical components typically found at synchrotron beamlines including a mirror for focusing the X-rays in the vertical direction and a reflection geometry Si (111) crystal that is bent to focus X-rays in the horizontal direction. We mentioned that the monochromator scattering plane was horizontal at X22A, whereas at X27A the monochromator scattering plane was vertical. The signal rates

were ~10 times lower than those obtainable at X27A, as we show in the experimental section below.

The reason for the decline in the signal rate at X22A compared to X27A is that the X-ray photon energy at X22A is by necessity within ±0.5 keV of 10 keV. At this low energy, the X-ray absorption by the sample is much larger than at 24.75 keV, the X-ray energy used at X27A. The reason why the X-ray energy range is restricted is the presence of focusing mirror. Although the primary purpose of this device is to focus the X-ray beam in the vertical direction (for single-crystal diffraction experiments), another purpose is to eliminate higher-order harmonics. For example the diffraction angle for the Si (111) reflection with 10 keV photons is identical to that of the Si (333) reflection with 30 keV photons, so with a source that contains a broad band of X-ray energies such as a synchrotron, both X-ray energies will be diffracted by the monochromator.[a] To remove these higher-order contaminants, the cutoff energy of the vertical focusing mirror was chosen to eliminate photon energies greater than ~15 keV.

Even though absorption of 10.3 keV X-rays by the battery cells examined was at least several orders of magnitude larger than that at 24.75 keV X-rays (see Fig. 2), the signal rates at X22A were down by only a factor of ~10 from those of X27A. This fortuitous situation occurred for a number of reasons: (*i*) the horizontal focusing available at X22A allowed the entire beam to illuminate the battery electrode, whereas at X27A only ~10% of the X-ray beam was utilized; (*ii*) the X-ray brightness of a bending magnet beamline source is ~10 times greater at 10.3 keV than 24.75 keV (see Fig. 1); (*iii*) the diffraction cross section is larger for 10.3 keV photons than 24.75 keV photons. All these factors helped make the experiments at X22A possible in spite of the much stronger absorption by the sample at 10.3 keV. Indeed if one replaces the LiF analyzer crystal with slits at X22A, signal rates comparable to those obtained at X27A are attainable, though the signal-to-background ratio is somewhat worse.

In situ cells and electrochemical aspects.—Lithium-ion rocking chair cells consisting of a carbon anode, a non-aqueous electrolyte and a $Li_xMn_2O_4$ cathode electrode with approximate dimensions 2 cm × 3 cm × 0.5 mm were manufactured by Gould Electronics. These were flat thin-layer single cells fabricated according to the specifications of the now familiar Bellcore technology.[13] The ratios of anode-to-cathode loadings of 1:1 were constant for all the cells, though the absolute loading, and hence the capacity varied from cell to cell. The electrolyte used was based on the Bellcore gel electrolyte concept[14] and comprised of a combination of ethylene carbonate (EC), dimethyl carbonate (DMC), and a $LiPF_6$ salt gelled using a polyvinylidene fluoride-hexafluoro propylene P(VDF-HFP) copolymers, the exact ratios being proprietary. Altogether six different Gould cells were examined, and all used the same electrolyte. Three were made using $Li_xMn_2O_4$ material from what we denote as batch-1, and the other three were made from what we denote as batch-2. Since the $Li_xMn_2O_4$ source was a commercial supplier, the differences in the preparation conditions of the two batches of the $Li_xMn_2O_4$ are proprietary. However, the methodology used for their preparation was based on procedures described in detail elsewhere.[2] The anode was comprised of a carbon coke from a proprietary source and was same for all of the cells. The anode and cathode electrodes were separately thermally laminated with copper and aluminum grids, respectively. They were then thermally fused together with the plastic electrolyte in a single cell. The cells were contained within sealed plastic bags. Being a commercial prototype, these cells did not have a built-in reference electrode. Hence the potentials cited in this paper correspond to the

---

[a] Higher-order contaminants can in principal be problematic with the setup used at X27A. With a Si (111) monochromator diffracting at 25 keV X-rays, the first harmonic is at 75 keV. The bending magnet photon flux at 75 keV is ~10,000 times smaller than at 25 keV, however, so harmonic contamination was not a problem for these experiments.

overall cell voltages. Its correlation with changes in the cathode material is however undeniable, since all other cell components remained unchanged. Because of the fused laminated structure the battery did not require any external pressure to ensure contact of components. The cells were sealed at the factory, and the X-ray diffraction experiments were performed on them with no modifications. The electrochemical state of the battery cells was controlled with a custom-made battery cycler interfaced with an IBM PC.

The fact that the cells used in this investigation were proprietary, together with the exact preparation conditions for the cathode material does not detract from the principle objective, which is to present the efficacy of using the synchrotron based in situ X-ray diffraction techniques in the transmission mode to investigate the structural evolution of cathode materials such as $Li_xMn_2O_4$ during intercalation and deintercalation of Li.

Results and Discussion

We first present in situ data that illustrate some of the advantages and disadvantages of transmission geometry X-ray diffraction techniques. Figure 4 shows typical transmission geometry X-ray diffraction data taken on a batch 2 material cell with 24.75 keV X-rays; this data has been presented in a previous publication[9] and is reproduced here only for completeness. This particular cell was charged to 4.25 V at the end of the fifth charge cycle, when the data were recorded. We have indexed the $Li_xMn_2O_4$ peaks visible in Fig. 4 to a cubic unit cell (space group Fd3m). The other peaks arise from the copper and aluminum grids, binding materials, the electrolyte and the cell container. We emphasize that the most intense $Li_xMn_2O_4$ peak, the (111) at $2\theta \sim 6°$, had a peak intensity of ~12000 counts/s under these conditions. This counting rate is comparable to those typically obtained in ex situ experiments with a conventional X-ray source, and allows the general structural behavior of the $Li_xMn_2O_4$ to be easily monitored. On the other hand, extraneous diffraction peaks and diffuse background scattering (such as broad peak at ~5° to ~8° in Fig. 6) can hinder detailed structural analysis such as Reitveld refinement. Interestingly, our transmission geometry data do not have substantially more background scattering than in situ experiments performed in a reflection geometry (see Fig. 3 in ref 8, for example).

We now consider the behavior of $Li_xMn_2O_4$ material during the initial charge cycle. The structural and electrochemical properties of cells made using two different batches of $Li_xMn_2O_4$ material are summarized in Fig. 5 and

6. The top panels of each figure show capacity vs. cell potential, and the bottom panel shows the corresponding $Li_xMn_2O_4$ lattice constant behavior. These data were calculated from the position of 2θ scans of the (531) and (511) Bragg peaks, assuming cubic structure (space group Fd3m). The batch-1 cell had higher anode and cathode loadings and hence a higher capacity than the batch-2 cell.

It is apparent from Fig. 5 and 6 that the properties of the cells made with two different batches of $Li_xMn_2O_4$ material are dramatically different. The behavior can nonetheless be divided into three distinct regions in both types of cell: (i) A region where the $Li_xMn_2O_4$ material is single phase with a monotonically contracting lattice constant. This region occurs from $x = 1$ to 0.45 in $Li_xMn_2O_4$, corresponding to a potential range of ~1.5 to 4.0 V in batch 1 and 2 type cells; (ii) A region where the $Li_xMn_2O_4$ exhibits the coexistence of two cubic phases with different lattice constants in batch-2 cells. In batch-1 cells, in this region, the diffraction peaks broaden but do not split into two distinct peaks. Here the x varies from 0.45 to 0.20 (corresponding potential range of ~3.7 to 4.05 V) in $Li_xMn_2O_4$ for both batch 1 and 2 type cells; (iii) A reemergence of the single-phase behavior that persists to the maximum potential to which the cells were charged, 4.3 V. This region occurs from $x = 0.20$ to ~0.02 (voltage range of ~4.05 to 4.23 V) for both batch 1 and 2 type cells.

We now consider in detail the X-ray scattering data from which the Fig. 5 and 6 were derived. Figure 7 shows the 2θ scans of $Li_xMn_2O_4$ (333), (511), (440), and (531) peaks in both types of cells for potential up to ~3 V. The data in the top panel of Fig. 7 is for a cell with batch-1 material and was recorded with 10.3 keV X-rays at X22A, and the data in the bottom panel is for a cell with batch-2 material and was recorded with 24.75 keV X-rays at X27A. The
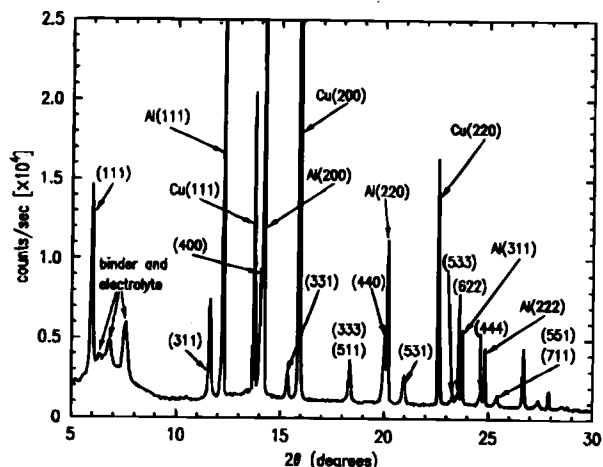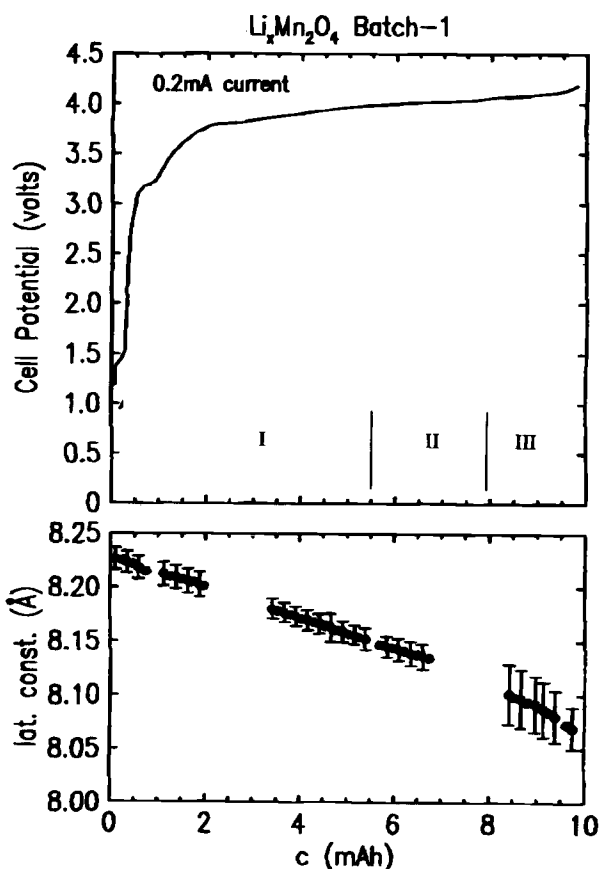
Fig. 4. 2θ scan taken on a lithium-ion cell, charged to 4.25 V in its fifth charge cycle. Peaks arising from aluminum, copper, binding materials, and electrolyte are labeled. The remaining indexed peaks arise from $Li_xMn_2O_4$ cathode material.

Fig. 5. Top panel: The potential as a function of capacity during the initial charge of a batch-1 cell. The charge rate used was C/50. Bottom panel: The corresponding $Li_xMn_2O_4$ lattice constants extracted from the position of the (531) peak(s). The closed circles and squares correspond to data recorded on two different batch-1 cells.
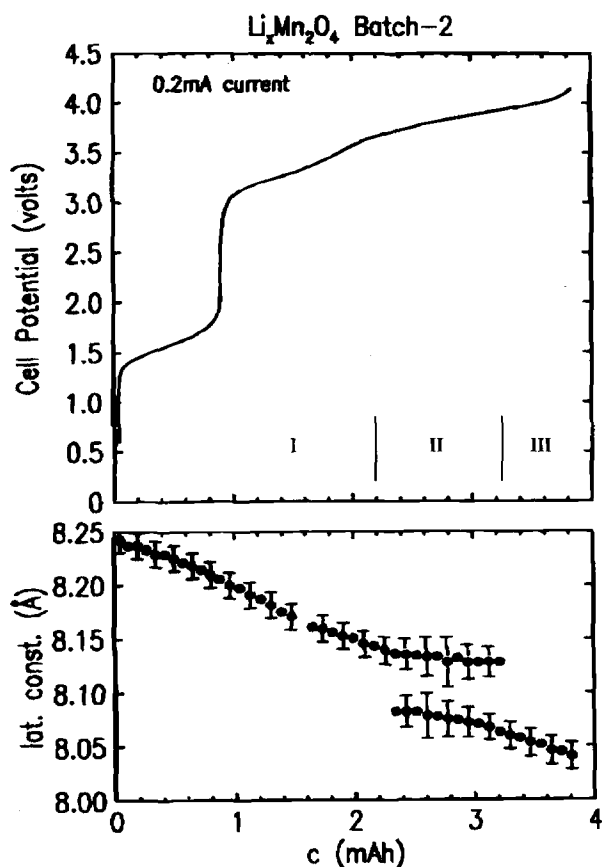
Fig. 6. Top panel: The potential as a function of capacity during the initial charge of a batch-2 cell. The charge rate used was C/20. Bottom panel: The corresponding $Li_xMn_2O_4$ lattice constants extracted from the position of the (531) peak(s). The material exhibited two-phase coexistence in region III where two lattice constant values are plotted at each capacity.

and (511) peaks are at the same value of 2θ ($\sim$18.2°), and the (333) and (511) peaks appear as a single peak, as in batch-1 scans in the top panel of Fig. 7. For the (333) and (511) peaks of fresh batch-2 material however, the single peak is split into at least three separate peaks as can be seen in the scans recorded at lower potentials in the bottom panel of Fig. 7. The (440) and the (531) peaks are considerably broadened at the lower potential as well. As charging progresses, the $Li_xMn_2O_4$ peaks in batch-2 material become narrower and their intensities increase showing the evolution into a single phase. The exact cause for these observed changes are not clear at this moment, however it does point to the power of this technique in terms of its superior resolution and true bulk in situ capability. This type of diagnostic ability is crucial for a better understanding of structural evolution in such spinel structures and is ultimately related to quality control.

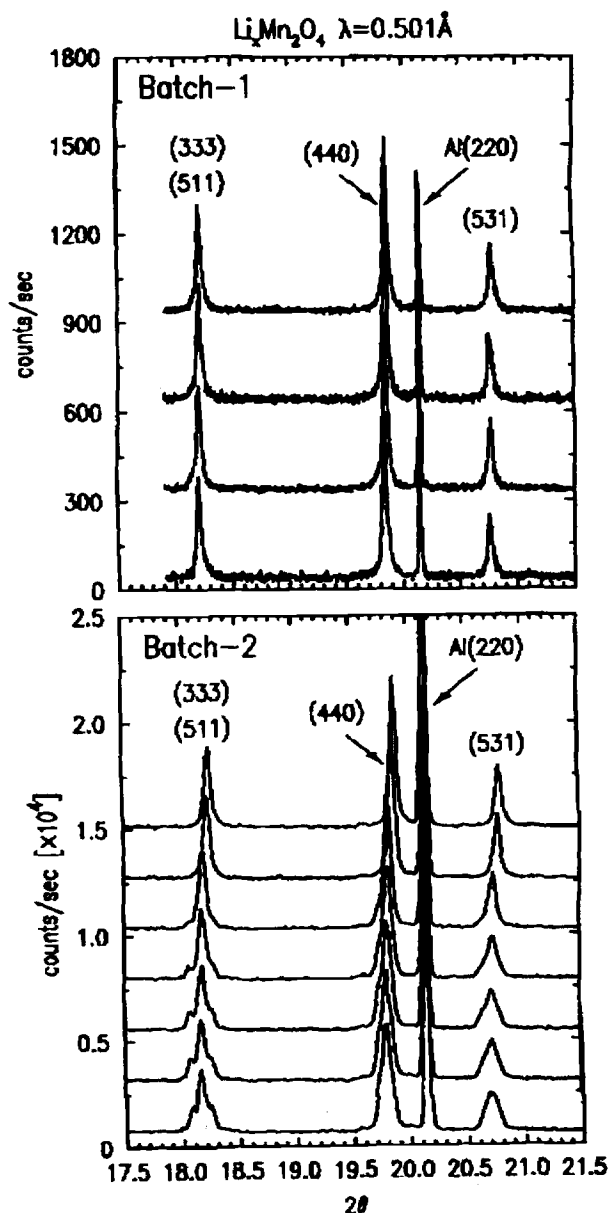In region II all of the $Li_xMn_2O_4$ peaks in batch-2 material split into two separate peaks in a manner consistent

2θ values of the 10.3 keV data have been converted to those appropriate for 24.75 keV X-rays to facilitate comparison of the data sets. We note that the peak intensities are sufficiently large that counting times of only one second were necessary for both data sets, but that the intensities of the $Li_xMn_2O_4$ peaks in the 24.75 keV data set are $\sim$10 times larger than those in the 10.3 keV data set.

Aluminum grid current collectors within the cell produced peaks in Fig. 7 at $2\theta \sim 20.15°$. These peaks were actually useful for this study, since they provided a convenient calibration of the spectrometer 2θ position (and hence a calibration of lattice constant values), as well as a measure of the 2θ resolution half-width. For the 24.75 keV data the resolution of the FWHM data was 0.034°, whereas that for the 10.3 keV data was 0.022° (after conversion of the 2θ angles to values appropriate for 24.75 keV X-rays). The spectrometer resolution is somewhat better for the 10.3 keV X-ray data set, but the resolution width at both X-ray energies is considerably narrower than any $Li_xMn_2O_4$ peaks in Fig. 7, so resolution effects are negligible here.

In region I of Fig. 5 and 6, batch-1 cells exhibit a small plateau at $\sim$1.5 V, whereas batch-2 cells exhibit a much larger plateau. The extent of this plateau was irreproducible, such a large $\sim$1.5 V plateau was not consistently seen in all batch-2 cells and $\sim$1.5 V plateaus larger than that shown in Fig. 5 were also observed in batch-1 cells. We therefore do not believe that the $\sim$1.5 V plateau is directly associated with structural changes in the $Li_xMn_2O_4$ starting materials. However, as shown on the bottom panel of Fig. 7, the structural characteristics of the batch-2 $Li_xMn_2O_4$ always evolved considerably in contrast to the batch-1 material. For a cubic structure, the (333)

Fig. 7. 2θ scans showing the evolution of the $Li_xMn_2O_4$ (511), (333), (440), and (531) peaks for batch-1 (top panel) and batch-2 (bottom panel) cells as potential varied from $\sim$1.37 to 3.00 V during the initial charge. The data for the cell from batch-1 were originally recorded with X-ray wavelength set at $\lambda = 1.1969$ Å, but the 2θ values have been converted to those corresponding to $\lambda = 0.5010$ Å X-rays for comparison.

with the coexistence of two cubic phases with different lattice constants. Examples of this behavior are illustrated in the bottom panel of Fig. 8, which shows a series of 2θ scans at the $Li_xMn_2O_4$ (531) peak. Two distinct peaks are clearly visible in the scans taken at $x = 0.34$ and 0.30 ($Li_xMn_2O_4$) in particular. This behavior is similar to that observed earlier by Ozhuku et al.[5] In batch-1 material, qualitatively similar behavior is observed, but there are important quantitative differences from the batch-2 behavior, as shown in the top panel of Fig. 8. Of most importance is that the (531) peak never completely separates into two distinct peaks as in the batch-1 material, but it does become significantly broader, which is suggestive of two overlapping peaks close to each other in 2θ. Thus, our batch-1 material appears to exhibit two-phase coexistence behavior during the initial charge cycle, but the effect is considerably smaller than in batch-2 material. This suppression of two-phase coexistence behavior has been previously reported by Xia and Yoshio[6] and Amatucci et al.[7] With further deintercalation, the two (531) peaks present in batch-2 material coalesce into one peak, and the single (531) peak present in batch-1 material narrows to its original width. We label this region where

a single cubic phase reappears, region III in Fig. 5 and 6. For the batch-1 cells, this single-phase behavior begins at $x = 0.10$ (~4.2 V), whereas for batch-2 cells it begins at $x = 0.14$ (~3.99 V). At the highest potential to which the cells were charged, 4.3 V, the batch-1 material lattice constant was 8.06 Å, whereas the batch-2 material lattice constant was somewhat smaller, 8.04 Å.

The large differences in the behavior of batch-1 and batch-2 cells suggest that some aspects of the battery performance are correlated to $Li_xMn_2O_4$ structural behavior. Indeed the experiments of Xia and Yoshio[6] suggest that two-phase coexistence behavior produces a decrease in the capacity during cycling. A plausible explanation for this correlation between structural behavior and cycle life arises from the nature of the structural transition. Because this transition is first order, it is likely that grains of $Li_xMn_2O_4$ are fractured during each charge/discharge cycle, which in turn could cause cell performance to deteriorate. In this scenario, the batch-2 cells would generally have poorer performance characteristics.

Conclusions

In conclusion, we have explained the procedures and rationale for performing in situ transmission geometry synchrotron X-ray diffraction measurements on battery cells, and demonstrated the utility of this technique in a preliminary study of $Li_xMn_2O_4$ structural behavior during the initial charge cycle. Our data indicate that secondary phases within some batches of $Li_xMn_2O_4$ cathode material convert into a single cubic phase at low potentials, and that the properties of the first-order structural phase transition into two-phase coexistence between $x = 0.45$ to 0.20 (~3.7 − 4.05 V) can vary dramatically in different batches of cathode material. Future in situ studies will examine $Li_xMn_2O_4$ structural phenomena under other operating conditions, such as after many charge/discharge cycles and after over-discharge.

Acknowledgments

Fig. 8. 2θ scans of the $Li_xMn_2O_4$ (531) peak in the two-phase coexistence region for cells from batch-1 (top panel) and batch-2 (bottom panel) cells recorded during the initial charge of the fresh cell. The data for the cell from batch-1 were originally recorded with X-ray wavelength set at $\lambda = 1.1969$ Å, but the 2θ values have been converted to those corresponding to $\lambda = 0.5010$ Å X-rays for comparison.

REFERENCES

1. M. M. Thakaray, A. de Kock, M. H. Rossouw, D. Liles, R. Bittihn, and D. Hoge, *This Journal*, **139**, 363 (1992).
2. J. M. Tarascon, W. R. McKinnon, F. Coowar, T. N. Bowmer, G. Amatucci, and D. Guyomard, *ibid.*, **141**, 1421 (1994).
3. A. Yamada, K. Miura, K. Hinokuma, and M. Tanaka, *ibid.*, **142**, 2149 (1995).
4. Y. Gao and J. R. Dahn, *ibid.*, **143**, 100 (1996).
5. T. Ozhuku, M. Kitagawa, and T. Hirai, *ibid.*, **137**, 769 (1990).
6. Y. Xia and M. Yoshio, *ibid.*, **143**, 825 (1996).
7. G. Amatucci, J. M. Tarascon, C. Schmultz, D. Larcher, T. Gozdz, and F. Shokoohi, Abstract 47, p. 57, The Electrochemical Society Meeting Abstracts, Vol. 96-1, Los Angeles, CA, May 5-10, 1996.
8. M. N. Richard, I. Koetschau, and J. R. Dahn, *This Journal*, **144**, 554 (1997).
9. W. Li, J. N. Reimers, and J. R. Dahn, *Solid State Ionics*, **67**, 123 (1993).
10. G. Amatucci, J. M. Tarascon, and L. C. Klein, *This Journal*, **143**, 1114 (1996).
11. T. R. Thurston, N. M. Jisrawi, S. Mukerjee, X. Q. Yang, J. McBreen, M. Daroux, and X. K. Xing, *Appl. Phys. Lett.*, **69**, 194 (1996).
12. P. Suortti, W. Thomlinson, D. Chapman, N. Gmur, D. P. Siddons, and C. Schulze, *Nucl. Instrum. Methods Phys. Res., Sect. A*, **336**, 304 (1993).
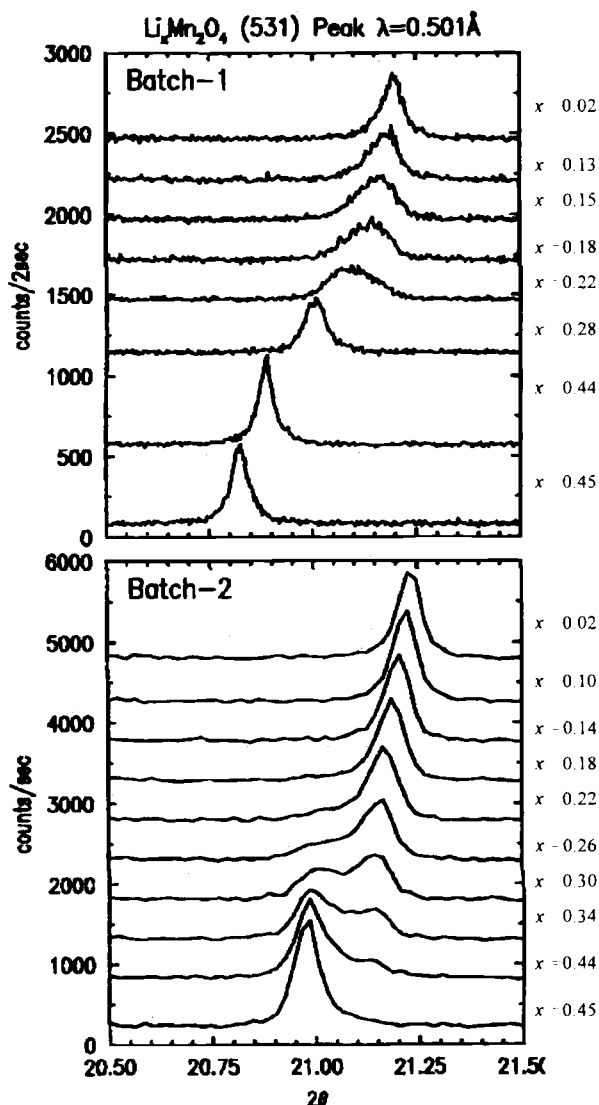
13. C. Schmutz, J. M. Tarascon, A. S. Gozdz, P. C. Warren, and F. K. Shokoohi, in *Rechargeable Lithium and Lithium ion Batteries*, S. M. Megahed, B. M. Barnett, L. Xie, Editors, PV 94-28, p. 330, The Electrochemi-cal Society Proceedings Series, Pennington, NJ (1994).

14. A. S. Gozdz, J. M. Tarascon, O. S. Gebizlioglu, C. N. Schmutz, P. C. Warren, and F. K. Shokoohi, *ibid.*, p. 400.

Differential Scanning Calorimetry Study of the Reactivity of Carbon Anodes in Plastic Li-Ion Batteries

A. Du Pasquier, F. Disma, T. Bowmer,[a] A. S. Gozdz,[a] G. Amatucci,[*,a] and J-M. Tarascon[*]

Laboratoire de Réactivité et de Chimie des Solides, URA CNRS 1211, Université de Picardie Jules Verne, 80039 Amiens Cedex, France

[a] *Bellcore, Red Bank, New Jersey 07701-7040, USA*

ABSTRACT

Chemical reactions taking place at elevated temperatures in a polymer-bonded lithiated carbon anode were studied by differential scanning calorimetry. The influences of parameters such as degree of intercalation, number of cycles, specific surface area, and chemical nature of the binder were elucidated. It was clearly established that the first reaction taking place at ca. 120–140 °C was the transformation of the passivation layer products into lithium carbonate, and that lithiated carbon reacted with the molten binder via dehydrofluorination only at $T > 300$ °C. Both reactions strongly depend on the specific surface area of the electrodes and the degree of lithiation.

Introduction

The difficulties in commercializing room temperature rechargeable batteries based on Li-metal anodes can be traced largely to safety problems associated with the reactivity of lithium metal. The dendritic growth of lithium during the recharge cycle can lead to electrical shorts through the separator and catastrophic failure of the battery. To circumvent the problems associated with the growth of lithium dendrites at the negative electrode and its high reactivity with the liquid-electrolyte components, metallic lithium in the negative electrode has been replaced by an intercalation compound having an electrochemical potential close to that of Li. A battery in which the lithium ions can be shuttled from one intercalation compound to another during charge and discharge of the cell is commonly known as a lithium-ion battery. Such a battery is inherently safer than a rechargeable Li-metal battery, since lithium is always confined to the ionic state (Li^+). Sony Energytec[1] was the first company to commercialize a Li-ion cell in 1991. These cells have since become key components of the portable, entertainment, computing, and telecommunications equipment in demand by an information-rich, mobile society. While safer, caution still has to be exercised to design a safe Li-ion battery. Responsibility for the safe use of this high-energy-content product is placed on everyone in the chain, from cell manufacturer to final user. If the cells using, for instance, $LiCoO_2$ as the positive electrode are overcharged (i.e., greater than $x = 0.5$ in Li_xCoO_2 of Li is removed), the positive and negative electrodes do not remain properly balanced. As a result, the excess Li has no sites available for intercalation in the negative electrode and plates as a metallic Li, which results in degraded cell performance and creates a safety hazard. These problems are even more important when charging groups of cells connected in series or when large-size batteries are used. For these reasons, additional safety features, such as electronic and thermally activated fuses, are built into each Li-ion battery pack.

Aiming to capitalize on the manufacturing advantages presented by polymer processing techniques, Bellcore researchers have introduced a novel process that uses plasticized polymeric electrolytes with a Li-ion system, thus developing the first reliable and practical rechargeable plastic Li-ion battery. Because of its flat shape (e.g., large heat-transfer area), such a battery may be safer than its liquid Li-ion counterpart in the case of an internal short. However, the stability of the poly(vinylidene fluoride) (PVDF)-type matrix in contact with Li metal has recently been questioned. At first it would seem that a Li-ion cell should not be affected by this issue, since it contains no Li metal. However, when a Li-ion cell is fully charged, the chemical activity of Li in the lithiated carbon electrode is close to that of lithium metal. Thus, a legitimate question arises with respect to the thermal stability of the lithiated carbon electrode containing PVDF as a binder. A recent study by Société des Accumulateurs Fixes et Tractés (SAFT) researchers[2] indicated that under certain conditions, lithiated carbon anodes may react violently with the PVDF binder. If so, it is important to know at what temperature this process may be initiated and what the chemical reactions involved are. The present study was undertaken to answer unambiguously these questions. The reaction of Li and Li_xC_6 with several PVDF-hexafluoropropene (HFP) compositions having various molecular weights, as well as with other polymers, such as poly(vinylchloride) (PVC) or polyacrylonitrile (PAN), was studied. The influence of the nature of carbon (graphite vs coke), its morphology (fibers vs sheets), and its surface area on the chemical reactivity of the lithiated carbon electrode with PVDF-HFP copolymers was also studied. We found that the reactivity of the PVDF matrix with the negative electrode increases as the degree of lithiation increases, independently of the nature of the precursor carbon; however, the reaction occurs only at temperatures higher than 300 °C.

Experimental

Samples of lithiated carbon anodes were prepared in Swagelok cells using a Whatman glass fiber separator and a Li metal counter electrode. Battery-grade electrolyte [1 M $LiPF_6$ in 2:1 v/v ethylene carbonate–dimethyl carbonate (EC-DMC), Merck, Darmstadt, Germany] was used as received. Carbon anodes were typically cast from 65 wt % MCMB 25-28 graphite (25 μm diam particles graphitized at 2800 °C, Osaka Gas Co., Osaka, Japan), 5 wt % Super P carbon black (MMM SA Carbon, Brussels, Belgium), 20 wt % dibutyl phthalate (DBP) plasticizer (Aldrich), and 10 wt % PVDF-HFP copolymer (Kynar FLEX 2801, Elf-Atochem America) according to a patented Bellcore process.[3] The DBP plasticizer was extracted with diethyl ether, resulting in a microporous electrode. The following solvents were used for casting plastic anodes: acetone for PVDF-HFP,